





## Article

# Effect of Varying $\text{AgNO}_3$ and $\text{CS}(\text{NH}_2)_2$ Concentrations on Performance of $\text{Ag}_2\text{S}/\text{ZnO}$ NRs/ITO Photoanode

Araa Mebdir Holi <sup>1,\*</sup>, Zulkarnain Zainal <sup>2,3</sup>, Asla A. Al-Zahrani <sup>4,\*</sup>, Asmaa Kadim Ayal <sup>5</sup>  
and Asmaa Soheil Najm <sup>6</sup>

<sup>1</sup> Department of Physics, College of Education, University of Al-Qadisiyah, Al-Qadisiyah, Al-Diwaniyah 58002, Iraq

<sup>2</sup> Materials Synthesis and Characterization Laboratory, Institute of Advanced Technology, Universiti Putra Malaysia, Selangor, Serdang 43400 UPM, Malaysia; zulkar@upm.edu.my

<sup>3</sup> Department of Chemistry, Faculty of Science, Universiti Putra Malaysia, Selangor, Serdang 43400 UPM, Malaysia

<sup>4</sup> Department of Chemistry, Faculty of Science, Imam Abdulrahman Bin Faisal University, Eastern Region, Dammam 34221, Saudi Arabia

<sup>5</sup> Department of Chemistry, College of Science for Women, University of Baghdad, Baghdad 10071, Iraq; asmaakaa\_chem@cs.w.uobaghdad.edu.iq

<sup>6</sup> Department of Electrical Electronic & Systems Engineering, Faculty of Engineering and Built Environment, Universiti Kebangsaan Malaysia, Selangor, Bangi 43600 UKM, Malaysia; asmaa.soheil@yahoo.com

\* Correspondence: araa.holi@qu.edu.iq (A.M.H.); aalazahrani@iau.edu.sa (A.A.A.-Z.); Tel.: +964-7823145910 (A.M.H.)

**Abstract:** This research focuses on improving the photoelectrochemical performance of binary heterostructure  $\text{Ag}_2\text{S}/\text{ZnO}$  NRs/ITO by manipulating synthesis conditions, particularly the concentrations of silver nitrate  $\text{AgNO}_3$  and thiourea  $\text{CS}(\text{NH}_2)_2$ . The photoelectrochemical performance of  $\text{Ag}_2\text{S}/\text{ZnO}$  nanorods on indium tin oxide (ITO) nanocomposite was compared to pristine ZnO NRs/ITO photoanode. The hydrothermal technique, an eco-friendly, low-cost method, was used to successfully produce  $\text{Ag}_2\text{S}/\text{ZnO}$  NRs at different concentrations of  $\text{AgNO}_3$  and  $\text{CS}(\text{NH}_2)_2$ . The obtained thin films were characterized using field emission scanning electron microscopy (FESEM), energy-dispersive X-ray spectroscopy (EDS), X-ray diffraction (XRD), ultraviolet-visible spectroscopy (UV-vis), and photoelectrochemical studies (PECs). We observed that there was an enhancement in absorbance in the visible region and effective photoelectron transfer between the  $\text{Ag}_2\text{S}/\text{ZnO}$  NRs/ITO photoelectrode and the electrolyte Red-Ox when illuminated with  $100 \text{ mW cm}^{-2}$ . Increasing the concentration of  $\text{AgNO}_3$  caused a remarkable decrease in the optical bandgap energy ( $E_g$ ) values. However, we noticed that there was an unstable trend in  $E_g$  when the concentration of  $\text{CS}(\text{NH}_2)_2$  was adjusted. The photoelectrochemical studies revealed that at a bias of 1.0 V, and 0.005 M of  $\text{AgNO}_3$  and 0.03 M of  $\text{CS}(\text{NH}_2)_2$ , the maximum photocurrent of the  $\text{Ag}_2\text{S}/\text{ZnO}$  NRs/ITO photoanode was  $3.97 \text{ mA/cm}^2$ , which is almost 11 times that of plain ZnO nanorods. Based on the outcomes of this investigating, the  $\text{Ag}_2\text{S}/\text{ZnO}$  NRs/ITO photoanode is proposed as a viable alternative photoanode in photoelectrochemical applications.

**Keywords:** varying  $\text{AgNO}_3$  and  $\text{CS}(\text{NH}_2)_2$  concentrations;  $\text{Ag}_2\text{S}/\text{ZnO}$  NRs/ITO photoanode; photoelectrochemical performance



**Citation:** Holi, A.M.; Zainal, Z.; Al-Zahrani, A.A.; Ayal, A.K.; Najm, A.S. Effect of Varying  $\text{AgNO}_3$  and  $\text{CS}(\text{NH}_2)_2$  Concentrations on Performance of  $\text{Ag}_2\text{S}/\text{ZnO}$  NRs/ITO Photoanode. *Energies* **2022**, *15*, 2950. <https://doi.org/10.3390/en15082950>

Academic Editors: Jae-Yup Kim and Jürgen Heinz Werner

Received: 31 January 2022

Accepted: 12 April 2022

Published: 18 April 2022

**Publisher's Note:** MDPI stays neutral with regard to jurisdictional claims in published maps and institutional affiliations.



**Copyright:** © 2022 by the authors. Licensee MDPI, Basel, Switzerland. This article is an open access article distributed under the terms and conditions of the Creative Commons Attribution (CC BY) license (<https://creativecommons.org/licenses/by/4.0/>).

## 1. Introduction

Due to their wide variety of applications in solar cells, photocatalysis, optoelectronics, and photoelectrochemical cells, semiconductor materials covered by another semiconductor layer, referred to as composite structures, are of great relevance [1–3]. Because of their energy gaps that extend the whole solar spectrum, semiconductor nanocomposites for PEC cell applications have attracted a lot of attention in the past 5 to 10 years [4–6]. Compared to single-crystal silicon cells, photoelectrochemical cells based on sensitized materials are less

costly to produce [7]. The optical, electrical, magnetic, and optoelectronic properties of semiconductors and their composites have been extensively studied to enhance them [8–10]. For the reasons stated below, Ag<sub>2</sub>S with ZnO were selected as semiconducting materials in our study. Ag<sub>2</sub>S, a direct bandgap semiconductor with a narrow bandgap (1.1 eV) that absorbs infrared light and exhibits optical absorption comparable to silicon, has piqued researchers' interest as a potential PEC cell material [11–14]. Additionally, it has been demonstrated that combining Ag<sub>2</sub>S with a wide bandgap semiconductor such as ZnO (that absorbs UV and near wavelengths) improves photovoltaic efficiency [15,16]. Due to its exceptional optical and electrical characteristics such as superb transparency and strong electron mobility, zinc oxide has been widely researched as a wide bandgap semiconductor (3.4 eV) and an inorganic material of the II–VI groups [17,18]. In this investigation, we sought to develop a method for making semiconductor composite materials that absorb electromagnetic spectra from UV to IR wavelengths, allowing us to improve the absorption of a wide scale of solar spectra with the same process. Two-component systems can produce three different types of heterostructures depending on the mutual arrangement of the energies of the electronic valence (VB) and conduction (CB) bands of semiconductors [19]. The type and direction of electron and hole transfer at heterojunctions induced by photoexcitation of the entire system or one of its components differ between these three heterostructures. Due to the charge separation at heterojunctions, which is a distinguishing feature of type II heterostructures, a review of the literature has revealed that the formation of type II heterostructured systems is one of the most common methods of increasing the efficiency of photocatalytic and photoelectrochemical systems [20,21]. According to investigations, we used ZnO as a broad bandgap semiconductor and Ag<sub>2</sub>S as a narrow bandgap semiconductor to make a semiconductor composite type II heterojunction [22,23]. This technique can improve ZnO's optoelectrical characteristics by promoting separation and suppressing recombination of hole–electron pairs formed in the material [24,25]. Chen and colleagues created the nano heterojunction core shell Ag<sub>2</sub>S/ZnO of a large spectrum range between 400 and 1100 nm with strong photosensitization [26]. ZnO nanostructures must be sensitized to boost their light absorption capability in addition to increasing their carrier generation. Numerous studies are reported to date on various ways to induce physical and chemical changes in ZnO surface properties using quantum dots (QDs) or doping of noble nanoparticles generated from metals. The benefits of these semiconductors include photo-stability, high extinction coefficients, and huge tunable energy gaps, which can be achieved by regulating particle sizes in quantum dot areas [27].

The most often used semiconductors, including CdS [28,29], CdSe [30,31], NiS [32], CdTe [33], and PbS [34], contain heavy metals such as cadmium (Cd) or lead (Pb). It is necessary to produce cd- or pb-free and more ecologically acceptable semiconductors so they can be employed for different applications in consumer products. As a result, several metal compounds are available, such as Ag<sub>2</sub>S [35], SnS [36], and Bi<sub>2</sub>S<sub>3</sub> [37], which have recently been investigated by many scientists. Ag<sub>2</sub>S has outstanding properties since it is a non-hazardous semiconductor with a direct bandgap, making it a useful material for a variety of applications [38,39]. A range of physical and chemical procedures have been used to deposit this metal sulfide as thin films [40,41]. Due to its excellent activity in the infrared absorption region, this metal compound can also produce a significant short-circuit current in the production of photoelectrochemical devices [42]. Furthermore, its high charge separation efficiency at the interface led to the use of Ag<sub>2</sub>S as a critical sensitizer in the PEC cell in conjunction with oxide anodes such as ZnO and NiO [17]. Despite this, only a few papers describe the fabrication of an Ag<sub>2</sub>S/ZnO photoanode. The hydrothermal deposition of Ag<sub>2</sub>S is dependent on the presence of silver and sulfide ions in the solution where the chemical deposition occurs,  $\text{CS}(\text{NH}_2)_2 + \text{H}_2\text{O} \leftrightarrow (\text{NH}_2)_2\text{CO} + \text{H}_2\text{S}$ ; after resale, H<sub>2</sub>S will be reacted with silver nitrate as  $2\text{AgNO}_3 + \text{H}_2\text{S} \rightarrow \text{Ag}_2\text{S} + 2\text{HNO}_3$ . This direct ion reactive technique can generate thin films without contaminants of very high quality [35,43]. For the deposition of Ag<sub>2</sub>S on the nanorods of ZnO, the hydrothermal technique has been used in this study. To identify prospective applications, various tests were carried out, including

the morphological, structural, and optical characteristics, and the photoelectrochemical performance of Ag<sub>2</sub>S/ZnO electrodes.

## 2. Materials and Methods

### 2.1. Preparation of Ag<sub>2</sub>S NPs/ZnO NRs

ZnO NRs were prepared by a two-step synthesis process: sol-gel spin coating and hydrothermal deposition. Sol-gel spin coating involved the coating of dense and uniform ZnO nanoparticle seed layer onto ITO substrates. Upon completing the heat treatment process of the seed layer, ZnO nanorods were grown on it by using the hydrothermal method. The hydrothermal growth was carried out at 90 °C for 4 h by using a water bath system [44]. The sealed glass container holding the ZnO NRs was submerged in an aqueous solution containing silver nitrate (AgNO<sub>3</sub>) and thiourea CS(NH<sub>2</sub>)<sub>2</sub> before being transferred to an oil bath. To study the effect of the precursor concentration of AgNO<sub>3</sub> in a fixed growth time of 25 min and temperature of 60 °C, the electrolyte comprising 0.03 M CS(NH<sub>2</sub>)<sub>2</sub> at various concentrations of AgNO<sub>3</sub> (0.001, 0.003, 0.005, 0.008, and 0.01) M was used, and then, the electrolyte comprising 0.005 M AgNO<sub>3</sub> at various concentrations of CS(NH<sub>2</sub>)<sub>2</sub> (10, 30, 50, 80, and 100) mM was investigated too. The Ag<sub>2</sub>S NPs/ZnO NRs/ITO photoanode was washed multiple times with DI to remove any residual salts and organic components on the surface of the film, followed by air drying.

### 2.2. Characterizations of Ag<sub>2</sub>S NPs/ZnO NRs

Field emission scanning electron microscopy (FESEM) was utilized to obtain the morphology of the samples, via JSM-7600F. The samples' structure was investigated by using an X-ray diffractometer (Panalytical X'Pert Pro MPD diffractometer) using Cu-K $\alpha$  radiation ( $\lambda = 1.54 \text{ \AA}$ ) at 40 kV and 40 mA. Lambda 20 ultraviolet-visible spectrophotometer was employed to evaluate the absorbance spectra of the prepared samples (Perkin Elmer Instruments).

### 2.3. Photoelectrochemical Performance of Ag<sub>2</sub>S NPs/ZnO NRs

In a conventional three-electrode cell system, the working electrodes were ZnO NRs/ITO and Ag<sub>2</sub>S/ZnO NRs/ITO nanocomposites, the reference electrode was Ag/AgCl, and the counter electrode was Pt wire. The photoelectrochemical parameters were measured using linear sweep voltammetry analysis, with a potentiostat Autolab PGSTAT204/FRA32M module controlling the potential and recording the corresponding photocurrent at a scan rate of 20 mV s<sup>-1</sup> in a solution of 0.1 M Na<sub>2</sub>S and 0.1 M Na<sub>2</sub>SO<sub>3</sub> electrolyte (pH = 13) under illumination at an intensity of 100 mW cm<sup>-2</sup> in the visible region (400–700 nm) of the electromagnetic spectrum generated by halogen lamp (Philips 13096 ELH GY 5.3 120 V). It is measured using a fiber optic spectrometer (Avaspec-2048).

## 3. Results

### 3.1. Part A: Effect of Varying AgNO<sub>3</sub> Concentrations

It is well known that increasing or decreasing the concentration of reactants will ultimately influence the resulting film. This implies that good control over the electrolyte composition can be employed to improve direct control over the final thin film. Figure 1 shows the Ag<sub>2</sub>S film morphology with a variation of the concentration of silver nitrate at a constant concentration of thiourea (0.03 M), with insets showing magnified top-view images for each sample. It can be noticed from Figure 1b that at a low concentration of 0.001 M of AgNO<sub>3</sub> with a high concentration of thiourea 0.03 M, the surface morphology displayed increasing diameter of the rods without any nanoparticles of Ag<sub>2</sub>S, which explained the XRD result presented in Figure 2. Meanwhile, Ag<sub>2</sub>S nanoparticles were successfully deposited on the surface of ZnO nanorods at a concentration of 0.003 M and a higher concentration of 0.005 M, with no noticeable change in the surface morphology of the two concentrations. The resulting films were homogenous and almost completely covered the whole surface of the ZnO NRs. However, as can be observed in Figure 1e–f, increasing the concentration of

$\text{AgNO}_3$  caused agglomeration of  $\text{Ag}_2\text{S}$  nanoparticles; subsequently, at high concentrations (0.008 M and 0.01 M) of  $\text{AgNO}_3$ , the rods merged due to the agglomeration of  $\text{Ag}_2\text{S}$  to form a continuous nanocomposite film. Furthermore, Figure 1f shows the presence of white spots on the surface. The spots are due to Ag protrusions which occurred spontaneously because of exposure to the electron beam. This phenomenon only occurred at a high concentration of  $\text{AgNO}_3$  and was noted by Morales Masis (2012) [45].

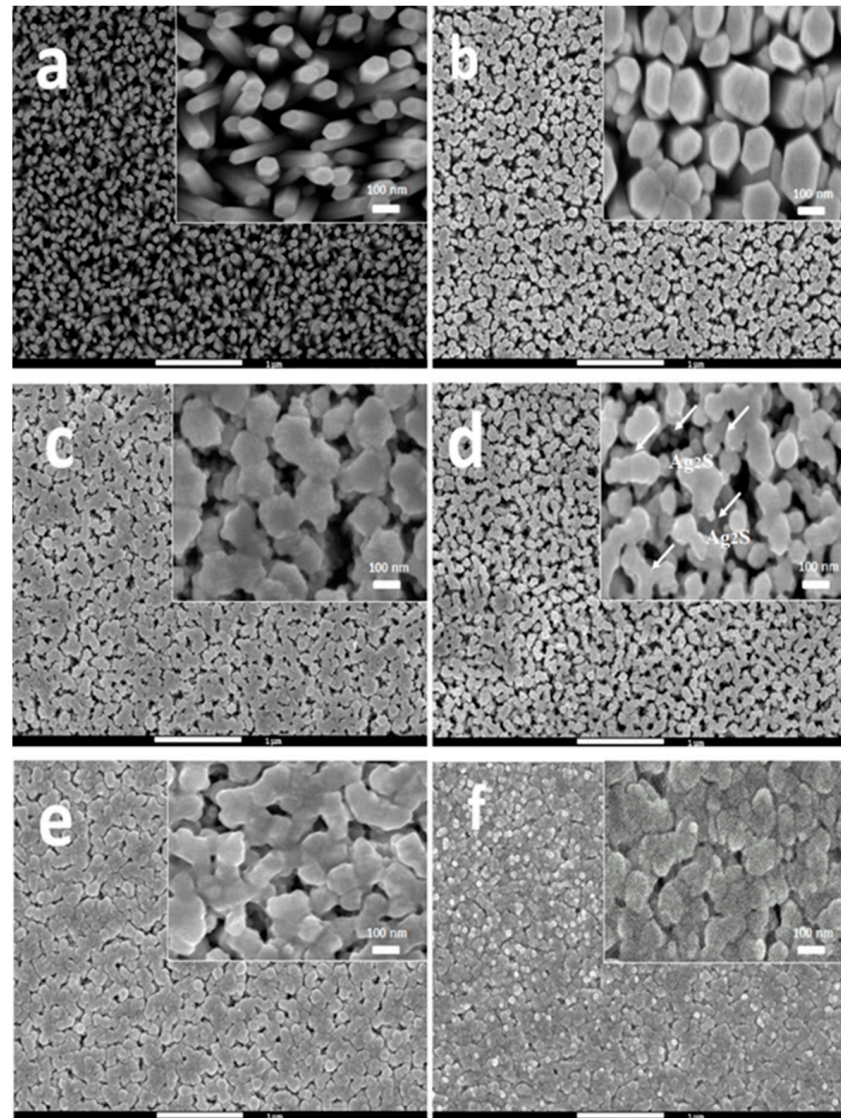


**Figure 1.** FESEM images of ZnO NRs (a);  $\text{Ag}_2\text{S}/\text{ZnO}$  NRs/ITO with various concentrations of  $\text{AgNO}_3$  (b) 0.001 M; (c) 0.003 M; (d) 0.005 M; (e) 0.008 M; and (f) 0.01 M. The figures' insets show the FESEM images at a higher magnification.

The phase compositions of ZnO NRs and  $\text{Ag}_2\text{S}/\text{ZnO}$  were obtained by XRD analysis. Figure 2a depicts the XRD pattern of bare ZnO NRs. Table 1 and Figure 2d–f index the monoclinic structure of  $\text{Ag}_2\text{S}$ , with the presence of impurities of elemental sulfur particularly at a concentration of 0.01 M, which shows a high intensity of  $\text{Ag}_2\text{S}$  peaks. This is also evident from the surface morphology analysis, which showed the agglomeration of nanoparticles. At a concentration of 0.001 M, no peaks corresponding to  $\text{Ag}_2\text{S}$  were observed. However, low-intensity peaks of ZnO were observed at a concentration of 0.001 M due to the presence of [thiourea silver thiocyanide  $\text{Ag}[\text{CS}(\text{NH}_2)_2]$  (SCN)] on the surface of ZnO.



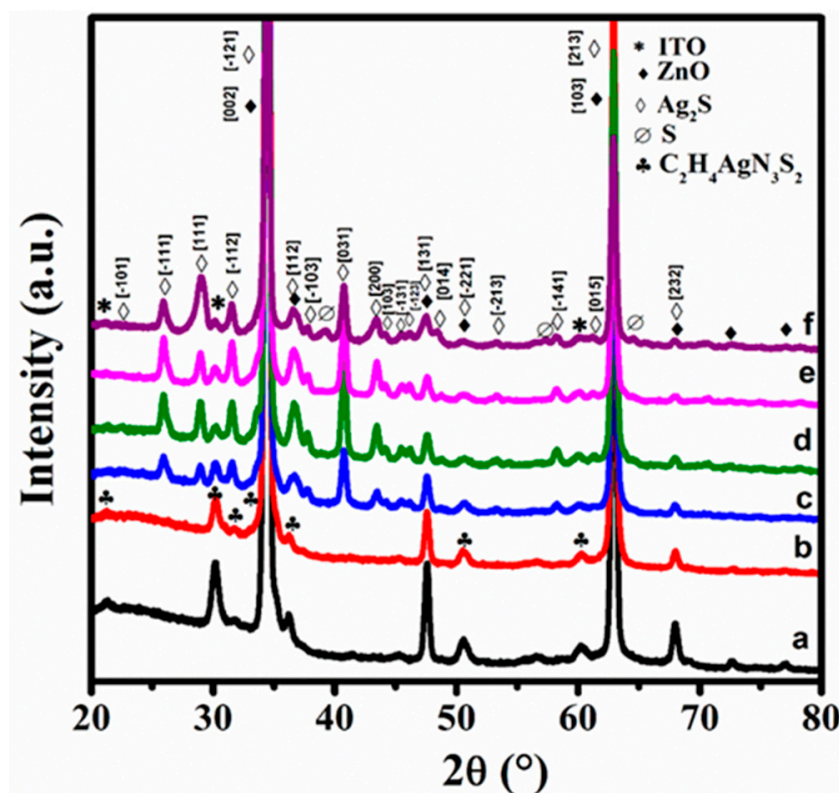


**Figure 2.** X-ray diffractogram of ZnO NRs (a), Ag<sub>2</sub>S/ZnO NRs/ITO with various concentrations of AgNO<sub>3</sub>: (b) 0.001 M; (c) 0.003 M; (d) 0.005 M; (e) 0.008 M; and (f) 0.01 M.

The optical characteristics of the Ag<sub>2</sub>S NPs/ZnO NRs nanocomposite were measured by a UV-visible spectrophotometer. The spectra of the samples are presented in Figure 3. These absorbance spectra revealed that the nanocomposite film Ag<sub>2</sub>S/ZnO has a high absorbance in a high concentration of AgNO<sub>3</sub> and the absorbance edge is seen to be strongly red-shifted. Moreover, it was exhibited that Ag<sub>2</sub>S NPs/ZnO NRs can absorb a wide range of light, including the infrared region. The absorption data are applied for evaluating the bandgap energy of the nanocomposite films, as presented in the insets of Figure 3. The optical bandgap energies values obtained are 3.20, 2.34, 2.21, 2.09, and 1.63 eV for Ag<sub>2</sub>S/ZnO thin films with 0.001, 0.003, 0.005, 0.008, and 0.01 M of AgNO<sub>3</sub>, respectively. It is observed that the energy gap decreases with the concentration of AgNO<sub>3</sub> due to the aggregation of particles. As also can be evident from the XRD result, at the concentration of 0.001 M of Ag<sup>+</sup>, the absorption is only limited to low wavelength (UV region).

Figure 4 shows the variation in the photocurrent at various AgNO<sub>3</sub> concentrations. At 0.001 M, a slight increase in photocurrent density is observed. This is consistent with the findings of FESEM and XRD data, which do not show a significant signal due to a very small amount of the Ag<sub>2</sub>S present in the surface of the nanorods. Furthermore, an increase in the concentration of AgNO<sub>3</sub> caused a higher increment in the photocurrent. The largest photocurrent density is obtained at a concentration of 0.005 M. However, at higher concentrations of 0.008 M and 0.01 M, the photoresponse dropped. This is due to the presence of elemental sulfur defects, which can also be observed in XRD Figure 2f, as well as white spots on the surface morphology, as seen in FESEM Figure 1f. As the concentration of Ag sources rises, the impurity scattering increases and causes a decrease in charge carrier mobility, resulting in poor interfacial charge carrier migration and a rise in the recombination rate of photoexcited electron–hole pairs. Thus, a concentration of AgNO<sub>3</sub> at 0.005 M was found preferable for Ag<sub>2</sub>S/ZnO hydrothermally deposition and was chosen for the following part.

**Table 1.** XRD data for Ag<sub>2</sub>S/ZnO NRs deposited at various concentrations of AgNO<sub>3</sub>.

Ag <sup>+</sup> Source	2θ (°)	D-Spacing (Å)		(hkl)	Compound
	Observed	Observed	Standard		
0.001 M	21.236	4.174	4.157	(040)	C <sub>2</sub> H <sub>4</sub> AgN <sub>3</sub> S <sub>2</sub>
	30.358	2.958	2.919	(140)	C <sub>2</sub> H <sub>4</sub> AgN <sub>3</sub> S <sub>2</sub>
	31.744	2.815	2.81	(131)	C <sub>2</sub> H <sub>4</sub> AgN <sub>3</sub> S <sub>2</sub>
	34.399	2.6	2.629	(052)	C <sub>2</sub> H <sub>4</sub> AgN <sub>3</sub> S <sub>2</sub>
	36.247	2.474	2.487	(15 $\bar{2}$ )	C <sub>2</sub> H <sub>4</sub> AgN <sub>3</sub> S <sub>2</sub>
	50.45	1.802	1.806	(054)	C <sub>2</sub> H <sub>4</sub> AgN <sub>3</sub> S <sub>2</sub>
	60.149	1.533	1.539	(116)	C <sub>2</sub> H <sub>4</sub> AgN <sub>3</sub> S <sub>2</sub>
0.003 M	-	-	3.96	( $\bar{1}$ 01)	Ag <sub>2</sub> S
	25.899	3.427	3.437	( $\bar{1}$ 11)	Ag <sub>2</sub> S
	28.128	3.069	3.08	(111)	Ag <sub>2</sub> S
	31.549	2.831	2.836	( $\bar{1}$ 12)	Ag <sub>2</sub> S
	40.658	2.217	2.213	(031)	Ag <sub>2</sub> S
	43.656	2.076	2.083	(200)	Ag <sub>2</sub> S
	45.501	1.996	1.995	( $\bar{1}$ 31)	Ag <sub>2</sub> S
46.193	1.964	1.963	( $\bar{1}$ 23)	Ag <sub>2</sub> S	
0.005 M	22.538	3.949	3.96	( $\bar{1}$ 01)	Ag <sub>2</sub> S
	25.871	3.441	3.437	( $\bar{1}$ 11)	Ag <sub>2</sub> S
	28.975	3.081	3.08	(111)	Ag <sub>2</sub> S
	31.618	2.833	2.836	( $\bar{1}$ 12)	Ag <sub>2</sub> S
	40.699	2.214	2.213	(031)	Ag <sub>2</sub> S
	43.458	2.083	2.083	(200)	Ag <sub>2</sub> S
	45.297	1.999	1.995	( $\bar{1}$ 31)	Ag <sub>2</sub> S
46.217	1.963	1.963	( $\bar{1}$ 23)	Ag <sub>2</sub> S	
0.008 M	-	-	3.96	( $\bar{1}$ 01)	Ag <sub>2</sub> S
	25.936	3.43	3.437	( $\bar{1}$ 11)	Ag <sub>2</sub> S
	28.902	3.08	3.08	(111)	Ag <sub>2</sub> S
	31.516	2.831	2.836	( $\bar{1}$ 12)	Ag <sub>2</sub> S
	40.783	2.211	2.213	(031)	Ag <sub>2</sub> S
	43.431	2.08	2.083	(200)	Ag <sub>2</sub> S
	45.512	1.99	1.995	( $\bar{1}$ 31)	Ag <sub>2</sub> S
46.174	1.965	1.963	( $\bar{1}$ 23)	Ag <sub>2</sub> S	
0.01 M	22.438	3.947	3.96	( $\bar{1}$ 01)	Ag <sub>2</sub> S
	25.937	3.433	3.437	( $\bar{1}$ 11)	Ag <sub>2</sub> S
	28.086	3.07	3.08	(111)	Ag <sub>2</sub> S
	31.535	2.829	2.836	( $\bar{1}$ 12)	Ag <sub>2</sub> S
	39.348	2.291	2.3	(0, 2, 10)	S
	40.748	2.218	2.213	(031)	Ag <sub>2</sub> S
	43.43	2.082	2.083	(200)	Ag <sub>2</sub> S
	45.529	1.989	1.995	( $\bar{1}$ 31)	Ag <sub>2</sub> S
	46.229	1.965	1.963	( $\bar{1}$ 23)	Ag <sub>2</sub> S
	57.308	1.608	1.61	(2, 2, 14)	S
	64.655	1.438	1.44	(5, 3, 11)	S

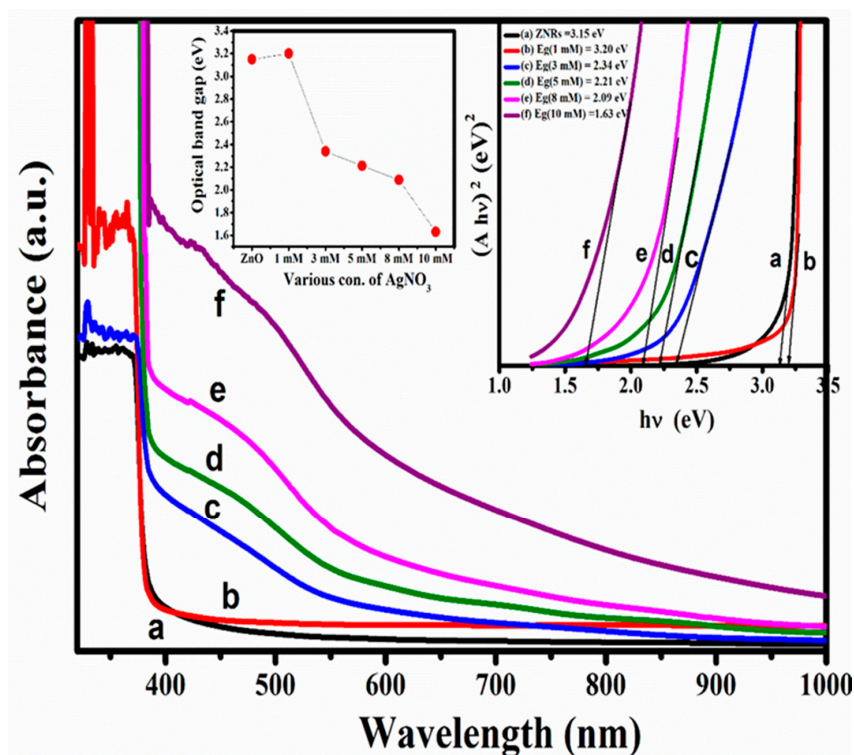


**Figure 3.** UV-visible spectra and Tauc plot for the direct allowed transitions (presented in insets of the figure) of ZnO NRs/ITO (a), and Ag<sub>2</sub>S/ZnO NRs/ITO prepared at various concentrations of AgNO<sub>3</sub>: (b) 0.001 M; (c) 0.003 M; (d) 0.005 M; (e) 0.008 M; and (f) 0.01 M.

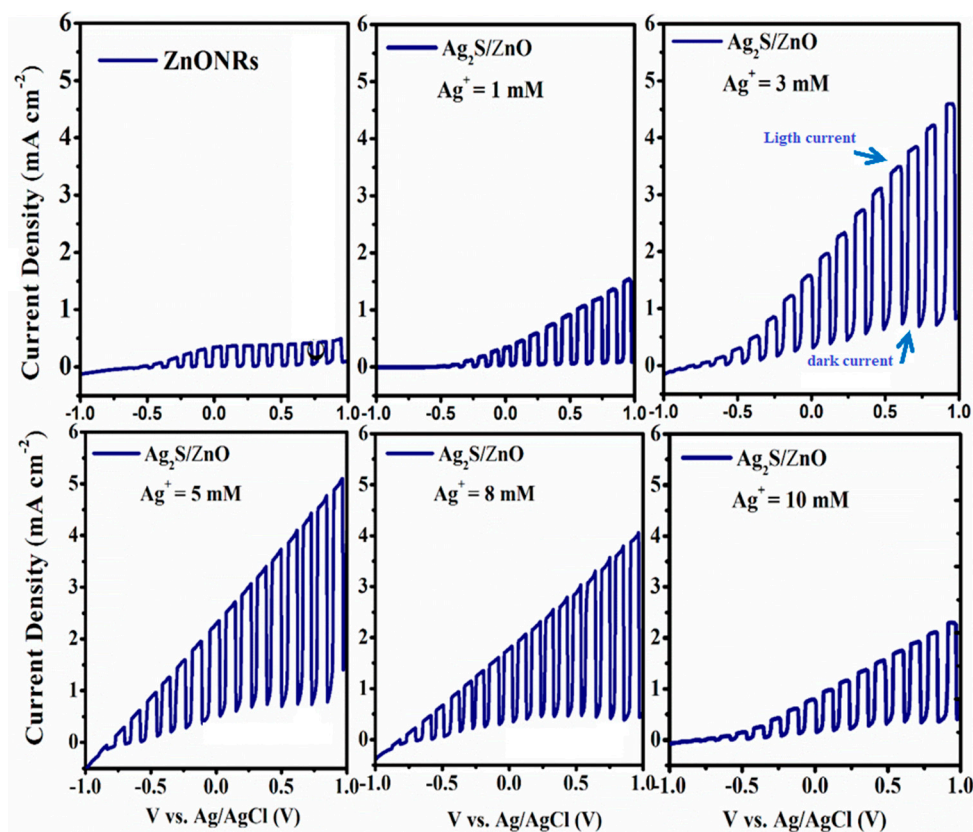


**Figure 4.** Linear sweep voltammograms from  $-1.0$  to  $1.0$  V at a scan rate of  $20 \text{ mV s}^{-1}$  for ZnO NRs/ITO and Ag<sub>2</sub>S/ZnO NRs/ITO formed at various AgNO<sub>3</sub> concentrations.



### 3.2. Part B: Effect of Varying $\text{CS}(\text{NH}_2)_2$ Concentration

To determine the effect of thiourea, the concentration was varied from 0.01 M to 0.1 M. The growth time, growth temperature, and precursor concentration of  $\text{AgNO}_3$  were fixed at 25 min, 60 °C, and 0.005 M, respectively.

Figure 5 displays FESEM images with insets that display magnified top-view images of each sample at various concentrations of thiourea. At a low concentration of 0.01 M, the films appeared smooth, with no occurrence of pinholes or cracks on the surface, as shown in Figure 5b. On other hand, at higher concentrations of thiourea (0.03 M and 0.05 M), it can be observed that the  $\text{Ag}_2\text{S}$  deposition rates on ZnO were relatively higher, and the uniform layer of  $\text{Ag}_2\text{S}$  NPs was formed. The deposited  $\text{Ag}_2\text{S}$  NPs finally covered whole ZnO NRs.

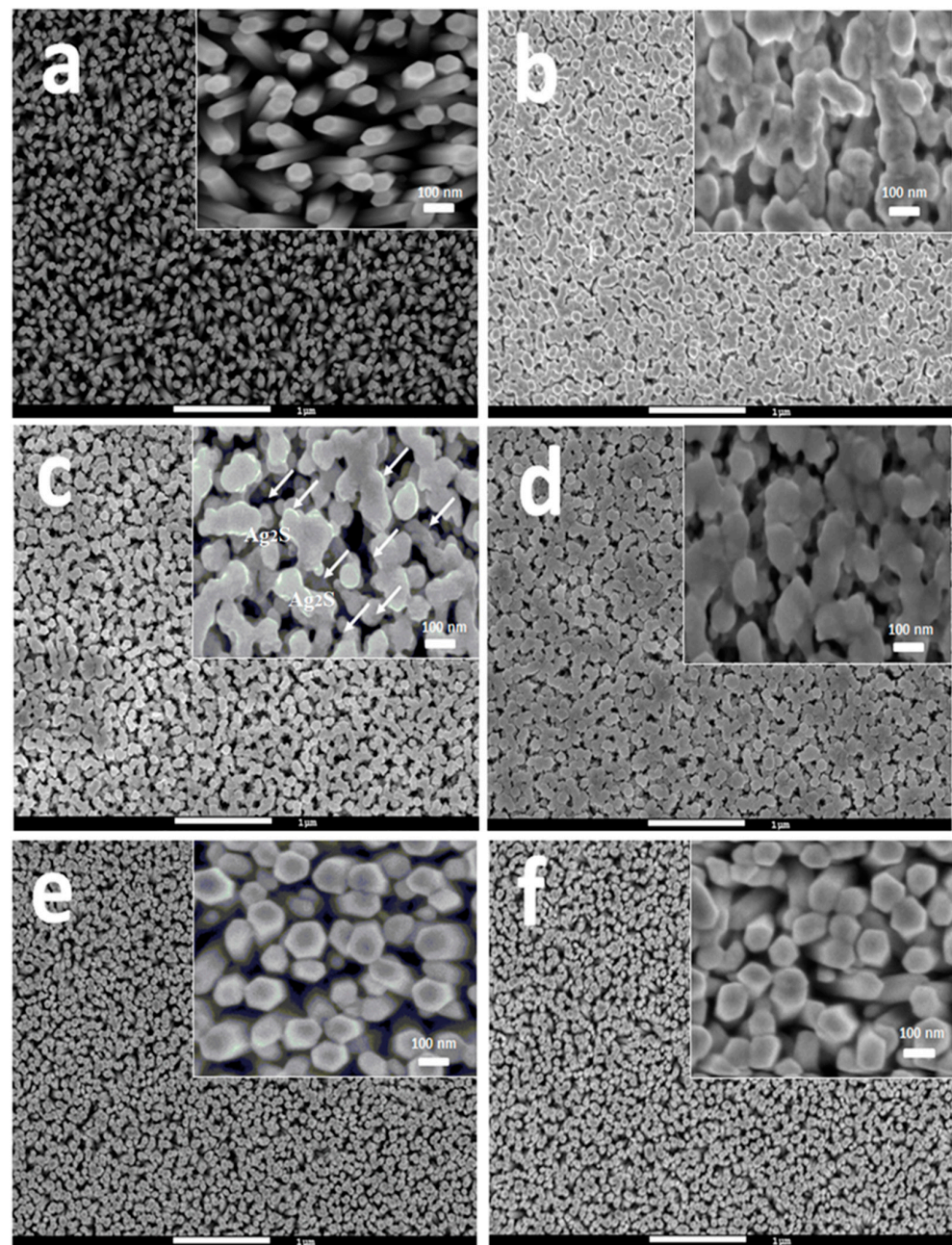


**Figure 5.** FESEM images of ZnO NRs (a);  $\text{Ag}_2\text{S}/\text{ZnO}$  NRs/ITO with various concentrations of  $\text{CS}(\text{NH}_2)_2$  (b) 0.01 M; (c) 0.03 M; (d) 0.05 M; (e) 0.08 M; and (f) 0.1 M. The figures' insets show the FESEM images at a higher magnification.



The FESEM images of hydrothermal deposited  $\text{Ag}_2\text{S}/\text{ZnO}$  at a higher concentration than 0.005 M are presented in Figure 5d,e. As shown from the morphology, no  $\text{Ag}_2\text{S}$  deposit was observed on ZnO NRs. The increase in the anion compound concentration above a certain limit led to the formation of precipitates leading to a lesser amount of  $\text{Ag}_2\text{S}$  deposited on the substrate. These observations were confirmed with the XRD result.

The formation of precipitates is given in the following equations (Nishimura, 2001) [46]:

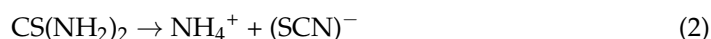


Figure 6 and Table 2 show the XRD results for hydrothermal deposited  $\text{Ag}_2\text{S}/\text{ZnO}$  films at various concentrations of  $\text{CS}(\text{NH}_2)_2$ . Figure 6 shows the XRD data for both bare ZnO NRs and  $\text{Ag}_2\text{S}/\text{ZnO}$  samples. As shown in Figure 6b,c, it is evident from XRD patterns of samples at concentrations 0.01 M, 0.03 M, and 0.05 M that the products formed were crystalline with no impurities. All peaks matched with either  $\text{Ag}_2\text{S}$  (JCPDS: 00-014-0072) or ZnO (JCPDS: 00-003-0888). This confirms that the material at these concentrations is  $\text{Ag}_2\text{S}$ . However, at a higher concentration of thiourea, no peaks for  $\text{Ag}_2\text{S}$  were found. Only lower intensity for ZnO was observed, presumably overlapping with the peaks for  $\text{Ag}[\text{CS}(\text{NH}_2)_2] (\text{SCN})$ . Solubility data and observations suggested that the soluble complexes  $\text{Ag}[\text{CS}(\text{NH}_2)_2]^+$  will form precipitation upon reaction with  $(\text{SCN})^-$  higher ratios of thiourea to silver nitrate, as commented by Nishimura (2001) [46] and James (1977) [47]. In this study, we noticed that there is an agreement between the X-ray results (Figure 6), which indicated the appearance of the complex compound upon a concentration of 0.001 M. As for the morphological images of the surface (Figure 5) for the same concentrations, it showed a difference from the other images. As for the UV-vis results, the curve showed clear shifting of the same concentrations mentioned.

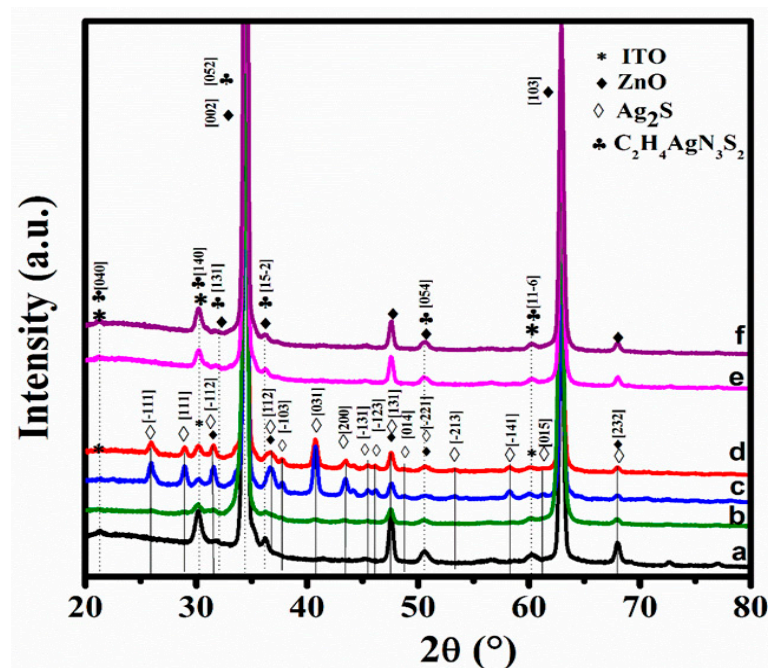
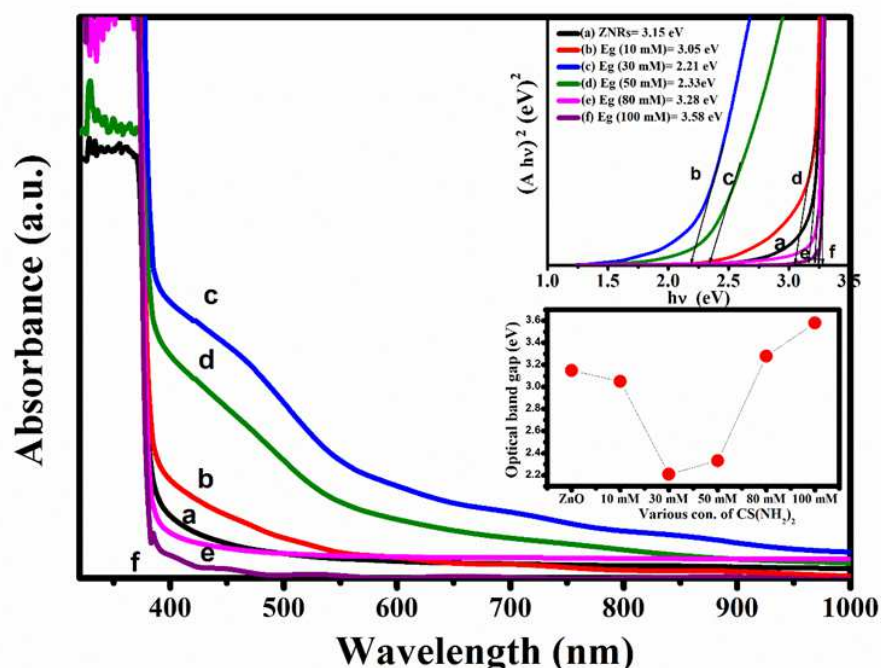


Figure 6. X-ray diffractogram of ZnO NRs (a),  $\text{Ag}_2\text{S}/\text{ZnO}$  NRs/ITO with various concentrations of  $\text{CS}(\text{NH}_2)_2$ : (b) 0.01 M; (c) 0.03 M; (d) 0.05 M; (e) 0.08 M; and (f) 0.1 M.

**Table 2.** XRD data for Ag<sub>2</sub>S/ZnO NRs deposited at various concentrations of CS(NH<sub>2</sub>)<sub>2</sub>.

S <sup>2-</sup> Source	2θ (°)		D-Spacing (Å)		(hkl)	Compound
	Observed	Observed	Observed	Standard		
0.01 M	-	-	-	3.96	( $\bar{1}01$ )	Ag <sub>2</sub> S
	26.047	3.421	3.437	3.437	( $\bar{1}11$ )	Ag <sub>2</sub> S
	-	-	-	3.08	(111)	Ag <sub>2</sub> S
	31.531	2.835	2.836	2.836	( $\bar{1}12$ )	Ag <sub>2</sub> S
	40.83	2.21	2.213	2.213	(031)	Ag <sub>2</sub> S
	43.452	2.078	2.083	2.083	(200)	Ag <sub>2</sub> S
	45.36	1.948	1.995	1.995	( $\bar{1}31$ )	Ag <sub>2</sub> S
	-	-	-	1.963	( $\bar{1}23$ )	Ag <sub>2</sub> S
0.03 M	22.538	3.949	3.96	3.96	( $\bar{1}01$ )	Ag <sub>2</sub> S
	25.871	3.441	3.437	3.437	( $\bar{1}11$ )	Ag <sub>2</sub> S
	28.975	3.081	3.08	3.08	(111)	Ag <sub>2</sub> S
	31.618	2.833	2.836	2.836	( $\bar{1}12$ )	Ag <sub>2</sub> S
	40.699	2.214	2.213	2.213	(031)	Ag <sub>2</sub> S
	43.573	2.083	2.083	2.083	(200)	Ag <sub>2</sub> S
	45.297	1.999	1.995	1.995	( $\bar{1}31$ )	Ag <sub>2</sub> S
	46.102	1.963	1.963	1.963	( $\bar{1}23$ )	Ag <sub>2</sub> S
0.05 M	-	-	-	3.96	( $\bar{1}01$ )	Ag <sub>2</sub> S
	25.96	3.435	3.437	3.437	( $\bar{1}11$ )	Ag <sub>2</sub> S
	28.95	3.076	3.08	3.08	(111)	Ag <sub>2</sub> S
	31.596	2.829	2.836	2.836	( $\bar{1}12$ )	Ag <sub>2</sub> S
	40.798	2.212	2.213	2.213	(031)	Ag <sub>2</sub> S
	43.443	2.08	2.083	2.083	(200)	Ag <sub>2</sub> S
	45.514	1.992	1.995	1.995	( $\bar{1}31$ )	Ag <sub>2</sub> S
	46.204	1.965	1.963	1.963	( $\bar{1}23$ )	Ag <sub>2</sub> S
0.08 M	21.236	4.18	4.157	4.157	(040)	C <sub>2</sub> H <sub>4</sub> AgN <sub>3</sub> S <sub>2</sub>
	30.246	2.949	2.919	2.919	(140)	C <sub>2</sub> H <sub>4</sub> AgN <sub>3</sub> S <sub>2</sub>
	-	-	2.81	2.81	(131)	C <sub>2</sub> H <sub>4</sub> AgN <sub>3</sub> S <sub>2</sub>
	34.52	2.602	2.629	2.629	(052)	C <sub>2</sub> H <sub>4</sub> AgN <sub>3</sub> S <sub>2</sub>
	36.253	2.474	2.487	2.487	(15 $\bar{2}$ )	C <sub>2</sub> H <sub>4</sub> AgN <sub>3</sub> S <sub>2</sub>
	50.577	1.806	1.806	1.806	(054)	C <sub>2</sub> H <sub>4</sub> AgN <sub>3</sub> S <sub>2</sub>
	60.28	1.534	1.539	1.539	(11 $\bar{6}$ )	C <sub>2</sub> H <sub>4</sub> AgN <sub>3</sub> S <sub>2</sub>
0.1 M	21.354	4.17	4.157	4.157	(040)	C <sub>2</sub> H <sub>4</sub> AgN <sub>3</sub> S <sub>2</sub>
	30.601	2.953	2.919	2.919	(140)	C <sub>2</sub> H <sub>4</sub> AgN <sub>3</sub> S <sub>2</sub>
	31.621	-	2.81	2.81	(131)	C <sub>2</sub> H <sub>4</sub> AgN <sub>3</sub> S <sub>2</sub>
	34.065	2.603	2.629	2.629	(052)	C <sub>2</sub> H <sub>4</sub> AgN <sub>3</sub> S <sub>2</sub>
	36.086	2.477	2.487	2.487	(152)	C <sub>2</sub> H <sub>4</sub> AgN <sub>3</sub> S <sub>2</sub>
	50.475	1.801	1.806	1.806	(054)	C <sub>2</sub> H <sub>4</sub> AgN <sub>3</sub> S <sub>2</sub>
	60.037	1.535	1.539	1.539	(11 $\bar{6}$ )	C <sub>2</sub> H <sub>4</sub> AgN <sub>3</sub> S <sub>2</sub>

The UV-vis spectra and the observed bandgap values of deposited Ag<sub>2</sub>S/ZnO nanocomposite for samples prepared at different concentrations of CS(NH<sub>2</sub>)<sub>2</sub> are given in Figure 7. The bandgap values of the sample prepared under concentrations of 0.01 M to 0.05 M lie in the range of 3.05 to 2.04 eV, indicating that they are shifted from a blue to red region when Ag<sub>2</sub>S was formed, which was also confirmed from the XRD results and FESEM. It is seen in insets Figure 7b,c that the value of the bandgap for the Ag<sub>2</sub>S/ZnO nanocomposite decreased with the increased concentration of thiourea. An above a concentration of 0.05 M which led to the low amount of Ag<sub>2</sub>S was created due to the precipitation effect as described earlier. Thus, bandgap values remain high close to the value of ZnO.



**Figure 7.** UV-vis spectra and Tauc plot for the direct allowed transitions (presented in insets of the figure) of ZnO NRs/ITO (a), and Ag<sub>2</sub>S/ZnO NRs/ITO prepared at various concentrations of CS(NH<sub>2</sub>)<sub>2</sub>: (b) 0.01 M; (c) 0.03 M; (d) 0.05 M; (e) 0.08 M; and (f) 0.1 M.

Under illumination, ZnO absorbs UV light and Ag<sub>2</sub>S absorbs visible light. The electrons and holes are generated in both ZnO and Ag<sub>2</sub>S. The photoexcited electrons from Ag<sub>2</sub>S will move to ZnO due to the lower conduction band (CB) of ZnO. Meanwhile, the holes of ZnO will migrate to Ag<sub>2</sub>S because of the higher valence band (VB) of Ag<sub>2</sub>S. The photoexcited electrons in ZnO move to ITO glass, then to the external wire, where they will be reduced at the counter electrode. On the surface/electrolyte, the photoexcited holes in Ag<sub>2</sub>S can oxidize. The photoexcited electron–hole pairs are effectively suppressed in this scenario, and the charge carrier lifetime in the ZnO/Ag<sub>2</sub>S heterostructure is extended. As a result, the photo response of Ag<sub>2</sub>/ZnO NRs is superior to pure ZnO. The amount of deposited Ag<sub>2</sub>S influences the photoelectrochemical properties of Ag<sub>2</sub>S NPs/ZnO NRs. PEC data (Figure 8) displayed only three photoelectrodes with the dark current, which is indicative of the presence of Ag<sub>2</sub>S/ZnO nanocomposite. Therefore, the optimal deposition and concentration for thiourea are important factors affecting the photoelectrochemical properties of Ag<sub>2</sub>S/ZnO NRs. The highest photocurrent was obtained for a thiourea concentration of 0.03 M.

The EIS analysis of photoelectrodes was performed to better explain the kinetics of the electrochemical and PEC processes occurring in the photoelectrodes. The photoelectrochemical EIS measurements were performed using a mixture of Na<sub>2</sub>S and Na<sub>2</sub>SO<sub>3</sub> electrolyte. The Nyquist plot for the PEC performance of ZnO NRs and Ag<sub>2</sub>S/ZnO NRs at optimum conditions (0.005 M AgNO<sub>3</sub> and 0.03 M CS(NH<sub>2</sub>)<sub>2</sub>) is shown in Figure 9. The Nyquist plot is used to measure the conductivity and charge transfer resistance [48]. It provides the qualitative insight of the charge transfer processes in bulk as well as at the interface of photoanode. From Figure 9, the arc diameter of Ag<sub>2</sub>S/ZnO NRs at optimum conditions (0.005 M AgNO<sub>3</sub> and 0.03 M CS(NH<sub>2</sub>)<sub>2</sub>) was smaller compared to the unmodified ZnO NRs photoanode, indicating the reduction in the resistance on the transport of charge. The Randle equivalent circuit contained the resistance of the solution ( $R_s$ ) related to the bulk properties of the electrolyte, the double-layer capacitance ( $C_{dl}$ ), and the charge transfer resistance ( $R_{ct}$ ) [49]. The last two are related to the surface properties of the interface between the electrode and the solution, and the fitting parameters are tabulated in Table 3. Accordingly,  $R_{ct}$  was  $12 \times 10^3$  and  $673 \Omega \cdot \text{cm}^2$  for pristine ZnO NRs and Ag<sub>2</sub>S/ZnO NRs,



respectively. The smallest  $R_{ct}$  of  $Ag_2S/ZnO$  NRs indicated higher conductivity and faster charge transformation at the interface on  $Ag_2S/ZnO$  NRs. This variation in  $R_{ct}$  values strongly supports PEC performance measurements [50]. Additionally, the different values of  $C_{dl}$  were attributed to the higher interface between  $Ag_2S/ZnO$  NRs and the electrolyte than that of pure ZnO NRs.

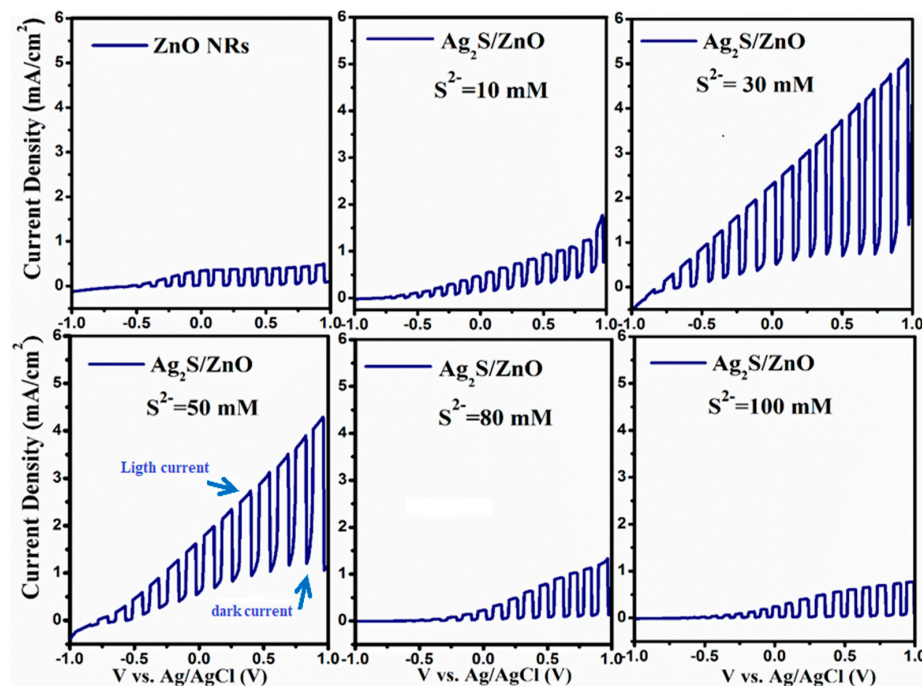


Figure 8. Linear sweep voltammograms from  $-1.0$  to  $1.0$  V at a scan rate of  $20$  mV  $s^{-1}$  for ZnO NRs/ITO and  $Ag_2S/ZnO$  NRs/ITO formed at various  $CS(NH_2)_2$  concentrations.

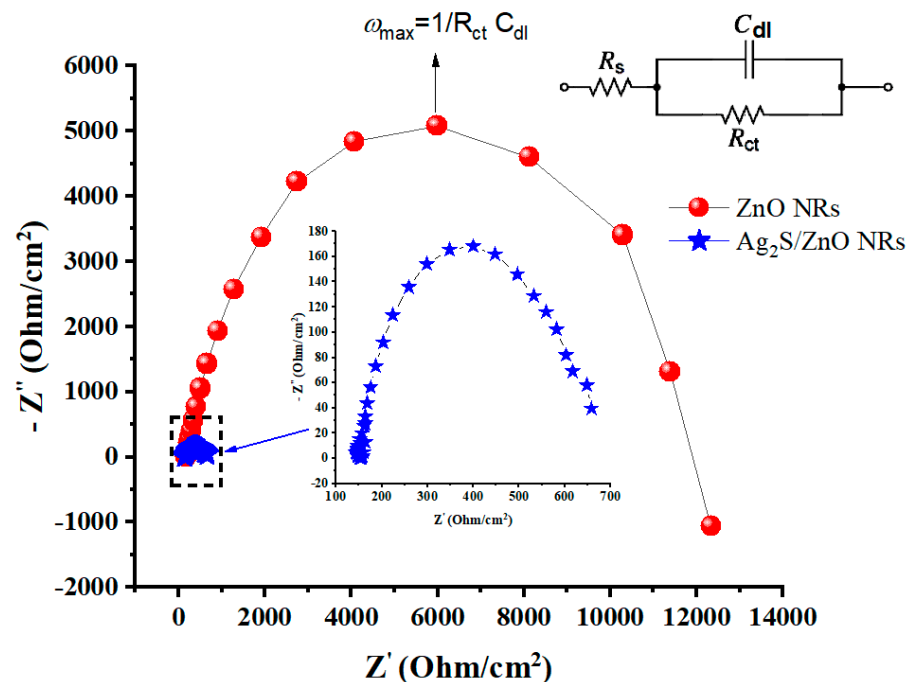


Figure 9. Nyquist plots (real  $Z$  vs. imaginary  $Z$ ) of plain ZnO NRs and optimal  $Ag_2S/ZnO$  NRs with concentrations of  $0.005$  M of  $AgNO_3$  and  $0.03$  M of  $CS(NH_2)_2$ . The inset is the simplified Randle circuit model employed to fit the Nyquist plot.  $\omega_{max} = 2\pi f_{max}$  is angular frequency,  $R_s$  is solution resistance,  $R_{ct}$  is charge transfer resistance, and  $C_{dl}$  is double-layer capacitance.

**Table 3.** Impedance spectroscopy analysis of photoanodes.

Photoanode Construction	$f_{\max}$ (mHz)	$R_{ct}$ ( $\Omega$ )	$R_s$ ( $\Omega$ )	$C_{dl}$ ( $\mu F$ )
ZnO NRs	45	$12 \times 10^3$	184	296
Ag <sub>2</sub> S <sub>3</sub> /ZnO NRs (Optimal sample)	295	673	153	802

It is well known that the conduction band (C.B.) and valance band (V.B.) of the narrow  $E_g$  semiconductor must be greater than the conduction band and valance band of ZnO NRs to enhance the transformation of the photogenerated electrons and holes. Considering the band structure of Ag<sub>2</sub>S and ZnO NRs, Figure 9 shows that both the valance band (1.56 eV) and conduction band (−0.65 eV) of Ag<sub>2</sub>S were greater than the conduction band (−0.29 eV) and valance band (2.9 eV) in ZnO NRs. Therefore, the electrons can transfer easily from the conduction band of Ag<sub>2</sub>S to the conduction band of ZnO NRs and promote the reduction reaction while the hole transfer occurs from ZnO to Ag<sub>2</sub>S due to the significant variance in the Fermi level alignment of the heterostructure.

The valance band (V.B.) and conduction band (C.B.) edge positions of Ag<sub>2</sub>S/ZnO NRs are estimated based on Equations:

$$E_{C.B.} = X - 0.5E_g + E_o \quad (5)$$

$$E_{V.B.} = E_{C.B.} + E_g \quad (6)$$

where  $E_{V.B.}$  is the valance band potential;  $E_{C.B.}$  is the conduction band potential;  $X$  is the semiconductor's electronegativity (which is the geometric mean of constituent atoms' electronegativity); the  $X$  values for ZnO and Ag<sub>2</sub>S are 5.79 eV and 4.96 eV, respectively;  $E_g$  is the semiconductor's bandgap energy; and  $E_o$  refers to the scaling factor describing the redox level of reference electrode to the vacuum ( $E_o = -4.5$  eV) for NHE. The  $E_g$  of bare ZnO and Ag<sub>2</sub>S/ZnO are calculated to be 3.15 and 2.21 eV, respectively [43]. From the earlier results, the Ag<sub>2</sub>S/ZnO/ITO exhibited a typical characteristic of type II heterojunctions, as demonstrated in Figure 10. The band alignment is useful to both the charge separation and collection, which leads to an enhanced photocurrent and a stronger oxidization capability towards PEC performance. Briefly, under the irradiation, the band offsets facilitate the enhancement of the charge separation, leading to a higher photocurrent value of the Ag<sub>2</sub>S/ZnO NRs electrode.

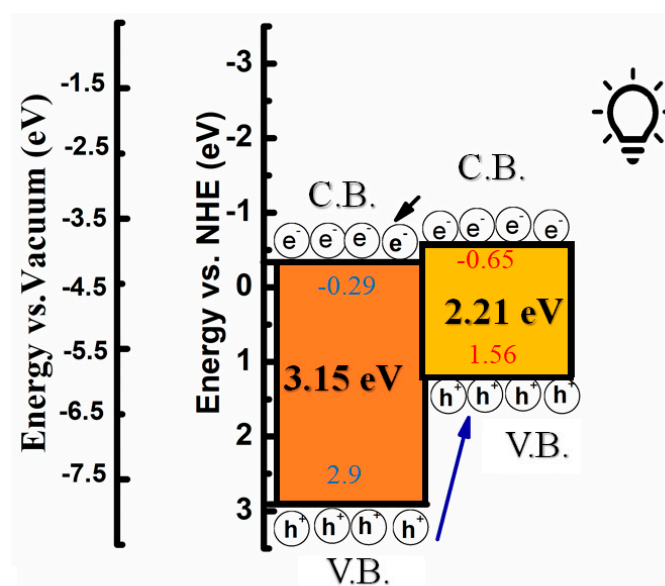


**Figure 10.** Schematic band alignment of optimal structure of Ag<sub>2</sub>S/ZnO NRs with concentrations of 0.005 M of AgNO<sub>3</sub> and 0.03 M of CS(NH<sub>2</sub>)<sub>2</sub>.

#### 4. Conclusions

In conclusion, we have effectively proved that the Ag<sub>2</sub>S/ZnO NRs photoanode can capture sunlight from the UV to visible light spectrum. FESEM, XRD, UV-vis, and PEC investigations were used to confirm the synthesis of Ag<sub>2</sub>S/ZnO heterostructures. The considerable absorption in the visible light region caused by Ag<sub>2</sub>S sensitization, as well as the successful separation of photoinduced carriers at the Ag<sub>2</sub>S/ZnO nanoheterojunction interface, are responsible for the large increase in photocurrent density. As a result of the optimization of concentration, which was found to be AgNO<sub>3</sub> concentration at 0.005 M and thiourea concentration of 0.03 M, the PEC of Ag<sub>2</sub>S/ZnO photoelectrode was improved. These findings demonstrate that Ag<sub>2</sub>S may be employed as an effective sensitizer, indicating that it can be considered as one of the most successful semiconductor materials to be used for solar energy harvesting as photoanodes of PEC cells, as a way to capture solar energy and store it as a translational energy source.

**Author Contributions:** Conceptualization, Z.Z. and A.M.H.; methodology, A.M.H.; software, A.K.A.; validation, A.A.A.-Z. and A.M.H.; formal analysis, A.S.N.; investigation, A.M.H.; resources, A.A.A.-Z.; data curation, Z.Z.; writing—original draft preparation, A.M.H.; writing—review and editing, A.A.A.-Z.; visualization, A.K.A.; supervision, Z.Z.; funding acquisition, Z.Z. and A.M.H. All authors have read and agreed to the published version of the manuscript.

**Funding:** This research was funded by the Malaysian Ministry of Education grant No. (0101-17-1912FR) and financial support of Araa Mebdir Holi from the Iraqi Ministry of Higher Education and Scientific Research.

**Institutional Review Board Statement:** Not applicable.

**Informed Consent Statement:** Not applicable.

**Conflicts of Interest:** The authors declare that they have no known competing financial interests or personal relationships that could have appeared to influence the work reported in this paper.

#### References

1. Bian, H.; Li, D.; Yan, J.; Liu, S.F. Perovskite—A wonder catalyst for solar hydrogen production. *J. Energy Chem.* **2021**, *57*, 325–340. [[CrossRef](#)]
2. Raj, J.S.; Sivaraman, P.; Prem, P.; Matheswaran, A. Wide Band Gap semiconductor material for electric vehicle charger. *Mater. Proc.* **2021**, *45*, 852–856.
3. Wang, F.; Li, Q.; Xu, D. Recent progress in semiconductor-based nanocomposite photocatalysts for solar-to-chemical energy conversion. *Adv. Energy Mater.* **2017**, *7*, 1700529. [[CrossRef](#)]
4. Cao, F.; Oskam, G.; Searson, P.C. A solid state, dye sensitized photoelectrochemical cell. *J. Phys. Chem.* **1995**, *99*, 17071–17073. [[CrossRef](#)]
5. Nayak, S.; Parida, K. Recent Progress in LDH@ Graphene and Analogous Heterostructures for Highly Active and Stable Photocatalytic and Photoelectrochemical Water Splitting. *Chem. Asian J.* **2021**, *16*, 2211–2248. [[CrossRef](#)]
6. Kim, J.H.; Hansora, D.; Sharma, P.; Jang, J.W.; Lee, J.S. Toward practical solar hydrogen production—An artificial photosynthetic leaf-to-farm challenge. *Chem. Soc. Rev.* **2019**, *48*, 1908–1971. [[CrossRef](#)]
7. Jiang, C.; Moniz, S.J.; Wang, A.; Zhang, T.; Tang, J. Photoelectrochemical devices for solar water splitting—materials and challenges. *Chem. Soc. Rev.* **2017**, *46*, 4645–4660. [[CrossRef](#)]
8. Awaid, T.J.; Ayal, A.K.; Farhan, A.M.; Sando, M.S.; Chin, L.Y. Effect of electrolyte composition on structural and photoelectrochemical properties of titanium dioxide nanotube arrays synthesized by anodization technique. *Baghdad Sci. J.* **2020**, *17*, 1183. [[CrossRef](#)]
9. AL-Zahrani, A.A.; Zainal, Z.; Talib, Z.A.; Lim, H.N.; Mohd Fudzi, L.; Holi, A.M. Synthesis of binary Bi<sub>2</sub>S<sub>3</sub>/ZnO nanorod array heterostructure and their photoelectrochemical performance. *J. Nanomater.* **2019**, *2019*, 5212938. [[CrossRef](#)]
10. Kumar, P.; Thakur, U.K.; Alam, K.; Kar, P.; Kisslinger, R.; Zeng, S.; Patel, S.; Shankar, K. Arrays of TiO<sub>2</sub> nanorods embedded with fluorine doped carbon nitride quantum dots (CNFQDs) for visible light driven water splitting. *Carbon* **2018**, *137*, 174–187. [[CrossRef](#)]
11. Al-Zahrani, A.A.; Zainal, Z.; Talib, Z.A.; Lim, H.N.; Holi, A.M.; Bahrudin, N.N. Enhanced photoelectrochemical performance of Bi<sub>2</sub>S<sub>3</sub>/Ag<sub>2</sub>S/ZnO novel ternary heterostructure nanorods. *Arab. J. Chem.* **2020**, *13*, 9166–9178. [[CrossRef](#)]
12. Guan, P.; Bai, H.; Wang, F.; Yu, H.; Xu, D.; Chen, B.; Xia, T.; Fan, W.; Shi, W. Boosting water splitting performance of BiVO<sub>4</sub> photoanode through selective surface decoration of Ag<sub>2</sub>S. *ChemCatChem* **2018**, *10*, 4927–4933. [[CrossRef](#)]



13. Zoha, S.; Ahmad, M.; Zaidi, S.J.; Ashiq, M.N.; Ahmad, W.; Park, T.J.; Basit, M.A. ZnO-based mutable Ag<sub>2</sub>S/Ag<sub>2</sub>O multilayered architectures for organic dye degradation and inhibition of E. coli and B. subtilis. *J. Photochem. Photobiol. A Chem.* **2020**, *394*, 112472. [[CrossRef](#)]
14. Orimolade, B.O.; Arotiba, O.A. Towards visible light driven photoelectrocatalysis for water treatment: Application of a FTO/BiVO<sub>4</sub>/Ag<sub>2</sub>S heterojunction anode for the removal of emerging pharmaceutical pollutants. *Sci. Rep.* **2020**, *10*, 5348. [[CrossRef](#)] [[PubMed](#)]
15. Chen, C.; Li, Z.; Lin, H.; Wang, G.; Liao, J.; Li, M.; Lv, S.; Li, W. Enhanced visible light photocatalytic performance of ZnO nanowires integrated with CdS and Ag<sub>2</sub>S. *Dalton Trans.* **2016**, *45*, 3750–3758. [[CrossRef](#)] [[PubMed](#)]
16. Tatarchuk, T.; Peter, A.; Al-Najar, B.; Vijaya, J.; Bououdina, M. Photocatalysis: Activity of nanomaterials. In *Nanotechnology in Environmental Science*; Hussain, C.M., Mishra, A.K., Eds.; Wiley-VCH: Weinheim, Germany, 2018; pp. 209–292.
17. Shafi, A.; Ahmad, N.; Sultana, S.; Sabir, S.; Khan, M.Z. Ag<sub>2</sub>S-sensitized NiO–ZnO heterostructures with enhanced visible light photocatalytic activity and acetone sensing property. *ACS Omega* **2019**, *4*, 12905–12918. [[CrossRef](#)]
18. Maevskaya, M.V.; Rudakova, A.V.; Koroleva, A.V.; Sakhatskii, A.S.; Emeline, A.V.; Bahnemann, D.W. Effect of the Type of Heterostructures on Photostimulated Alteration of the Surface Hydrophilicity: TiO<sub>2</sub>/BiVO<sub>4</sub> vs. ZnO/BiVO<sub>4</sub> Planar Heterostructured Coatings. *Catalysts* **2021**, *11*, 1424. [[CrossRef](#)]
19. Enesca, A.; Isac, L. Tuned S-Scheme Cu<sub>2</sub>S\_TiO<sub>2</sub>\_WO<sub>3</sub> Heterostructure Photocatalyst toward S-Metolachlor (S-MCh) Herbicide Removal. *Materials* **2021**, *14*, 2231. [[CrossRef](#)]
20. Adachi, S. *Properties of Semiconductor Alloys: Group-IV, III–V and II–VI Semiconductors*; John Wiley & Sons: New York, NY, USA, 2009.
21. Li, D.; Wu, W.; Zhao, Y.; Qiao, R. Type-II heterojunction constructed by Ag<sub>2</sub>S-coupled ZnO microspheres with visible light-responsive antibacterial activity. *Mater. Lett.* **2020**, *271*, 127709. [[CrossRef](#)]
22. Jin, Y.; Jiao, S.; Wang, D.; Gao, S.; Wang, J. Enhanced UV Photoresponsivity of ZnO Nanorods Decorated with Ag<sub>2</sub>S/ZnS Nanoparticles by Successive Ionic Layer Adsorption and Reaction Method. *Nanomaterials* **2021**, *11*, 461. [[CrossRef](#)]
23. Subash, B.; Krishnakumar, B.; Pandiyan, V.; Swaminathan, M.; Shanthi, M. An efficient nanostructured Ag<sub>2</sub>S–ZnO for degradation of Acid Black 1 dye under day light illumination. *Sep. Purif. Technol.* **2012**, *96*, 204–213. [[CrossRef](#)]
24. Adnan, M.A.; Julkapli, N.M.; Abd Hamid, S.B. Review on ZnO hybrid photocatalyst: Impact on photocatalytic activities of water pollutant degradation. *Rev. Inorg. Chem.* **2016**, *36*, 77–104.
25. Su, T.; Shao, Q.; Qin, Z.; Guo, Z.; Wu, Z. Role of interfaces in two-dimensional photocatalyst for water splitting. *ACS Catal.* **2018**, *8*, 2253–2276. [[CrossRef](#)]
26. Chen, D.; Wei, L.; Wang, D.; Chen, Y.; Tian, Y.; Yan, S.; Mei, L.; Jiao, J. Ag<sub>2</sub>S/ZnO core-shell nanoheterojunction for a self-powered solid-state photodetector with wide spectral response. *J. Alloy. Compd.* **2018**, *735*, 2491–2496. [[CrossRef](#)]
27. Arakawa, Y.; Holmes, M.J. Progress in quantum-dot single photon sources for quantum information technologies: A broad spectrum overview. *Appl. Phys. Rev.* **2020**, *7*, 021309. [[CrossRef](#)]
28. Holi, A.M.; Zainal, Z.; Talib, Z.A.; Lim, H.N.; Yap, C.C.; Chang, S.K.; Ayal, A.K. Hydrothermal deposition of CdS on vertically aligned ZnO nanorods for photoelectrochemical solar cell application. *J. Mater. Sci. Mater. Electron.* **2016**, *27*, 7353–7360. [[CrossRef](#)]
29. Ayal, A.K. Enhanced photocurrent of titania nanotube photoelectrode decorated with CdS nanoparticles. *Baghdad Sci. J.* **2018**, *15*, 57–62.
30. Ayal, A.K.; Zainal, Z.; Holi, A.M.; Lim, H.N.; Talib, Z.A.; Lim, Y.C. Sensitization of TiO<sub>2</sub> nanotube arrays photoelectrode via homogeneous distribution of CdSe nanoparticles by electrodeposition techniques. *J. Phys. Chem. Solids* **2021**, *153*, 110006. [[CrossRef](#)]
31. Li, Z.; Jin, D.; Wang, Z. ZnO/CdSe-diethylenetriamine nanocomposite as a step-scheme photocatalyst for photocatalytic hydrogen evolution. *Appl. Surf. Sci.* **2020**, *529*, 147071. [[CrossRef](#)]
32. Zhang, Q.; Xiao, Y.; Li, Y.; Zhao, K.; Deng, H.; Lou, Y.; Chen, J.; Cheng, L. NiS-Decorated ZnO/ZnS Nanorod Heterostructures for Enhanced Photocatalytic Hydrogen Production: Insight into the Role of NiS. *Sol. RRL* **2020**, *4*, 1900568. [[CrossRef](#)]
33. Liu, Y.; Chen, F.; Li, Q.; Bao, H. Synthesis of CdTe/Carbon nanotube/ZnO flower-like micro-spheres and their photocatalytic activities in degradation of rohdamine B. *Mater. Lett.* **2018**, *210*, 23–25. [[CrossRef](#)]
34. Holi, A.M.; Al-Zahrani, A.A.; Najm, A.S.; Chelvanathan, P.; Amin, N. PbS/CdS/ZnO nanowire arrays: Synthesis, structural, optical, electrical, and photoelectrochemical properties. *Chem. Phys. Lett.* **2020**, *750*, 137486. [[CrossRef](#)]
35. Holi, A.M.; Zainal, Z.; Ayal, A.K.; Chang, S.K.; Lim, H.N.; Talib, Z.A.; Yap, C.C. Ag<sub>2</sub>S/ZnO nanorods composite photoelectrode prepared by hydrothermal method: Influence of growth temperature. *Optik* **2019**, *184*, 473–479. [[CrossRef](#)]
36. Jayswal, S.; Moirangthem, R.S. Construction of a solar spectrum active SnS/ZnO p–n heterojunction as a highly efficient photocatalyst: The effect of the sensitization process on its performance. *New J. Chem.* **2018**, *42*, 13689–13701. [[CrossRef](#)]
37. AL-Zahrani, A.A.; Zainal, Z.; Talib, Z.A.; Lim, H.N.; Holi, A.M. Study the Effect of the Heat Treatment on the Photoelectrochemical Performance of Binary Heterostructured Photoanode Ag<sub>2</sub>S/ZnO Nanorod Arrays in Photoelectrochemical Cells. *Mater. Sci. Forum* **2020**, *1002*, 187–199. [[CrossRef](#)]
38. Lei, Y.; Jia, H.; He, W.; Zhang, Y.; Mi, L.; Hou, H.; Zhu, G.; Zheng, Z. Hybrid solar cells with outstanding short-circuit currents based on a room temperature soft-chemical strategy: The case of P3HT: Ag<sub>2</sub>S. *J. Am. Chem. Soc.* **2012**, *134*, 17392–17395. [[CrossRef](#)]
39. Sadovnikov, S.I.; Gusev, A.I. Recent progress in nanostructured silver sulfide: From synthesis and nonstoichiometry to properties. *J. Mater. Chem. A* **2017**, *5*, 17676–17704. [[CrossRef](#)]

40. Sankapal, B.R.; Mane, R.S.; Lokhande, C.D. A new chemical method for the preparation of Ag<sub>2</sub>S thin films. *Mater. Chem. Phys.* **2000**, *63*, 226–229. [[CrossRef](#)]
41. Zamiri, R.; Abbastabar Ahangar, H.; Zakaria, A.; Zamiri, G.; Shabani, M.; Singh, B.; Ferreira, J.M. The structural and optical constants of Ag<sub>2</sub>S semiconductor nanostructure in the Far-Infrared. *Chem. Cent. J.* **2015**, *9*, 28. [[CrossRef](#)]
42. Xue, J.; Liu, J.; Liu, Y.; Li, H.; Wang, Y.; Sun, D.; Wang, W.; Huang, L.; Tang, J. Recent advances in synthetic methods and applications of Ag<sub>2</sub>S-based heterostructure photocatalysts. *J. Mater. Chem. C* **2019**, *7*, 3988–4003. [[CrossRef](#)]
43. Holi, A.M.; Zainal, Z.; Ayal, A.K.; Chang, S.K.; Lim, H.N.; Talib, Z.A.; Yap, C.C. Effect of heat treatment on photoelectrochemical performance of hydrothermally synthesised Ag<sub>2</sub>S/ZnO nanorods arrays. *Chem. Phys. Lett.* **2018**, *710*, 100–107. [[CrossRef](#)]
44. Holi, A.M.; Zainal, Z.; Talib, Z.A.; Lim, H.N.; Yap, C.C.; Chang, S.K.; Ayal, A.K. Effect of hydrothermal growth time on ZnO nanorod arrays photoelectrode performance. *Optik* **2016**, *127*, 11111–11118. [[CrossRef](#)]
45. Morales Masis, M. *Resistive Switching in Mixed Conductors: Ag<sub>2</sub>S as a Model System*; Leiden University: Leiden, The Netherlands, 2012.
46. Nishimura, D. Report on the Chemical Treatment of Photographic Materials Workshop: A Chemist's Perspective. *Top. Photogr. Preserv.* **2001**, *9*, 1–43.
47. James, T.H. *The Theory of the Photographic Process*; Macmillan: New York, NY, USA, 1966.
48. Liu, Y.; Yan, X.; Kang, Z.; Li, Y.; Shen, Y.; Sun, Y.; Wang, L.; Zhang, Y. Synergistic effect of surface plasmonic particles and surface passivation layer on ZnO nanorods array for improved photoelectrochemical water splitting. *Sci. Rep.* **2016**, *6*, 29907. [[CrossRef](#)]
49. Kumar, S.; Ahirwar, S.; Satpati, A.K. Insight into the PEC and interfacial charge transfer kinetics at the Mo doped BiVO<sub>4</sub> photoanodes. *RSC Adv.* **2019**, *9*, 41368–41382. [[CrossRef](#)]
50. Yavarinasab, A.; Abedini, M.; Tahmooressi, H.; Janfaza, S.; Tasnim, N.; Hoorfar, M. Potentiodynamic Electrochemical Impedance Spectroscopy of Polyaniline-Modified Pencil Graphite Electrodes for Selective Detection of Biochemical Trace Elements. *Polymers* **2021**, *14*, 31. [[CrossRef](#)]